Extended Canadian middle atmosphere model: zonal-mean climatology and physical parameterizations

Article

Published Version

Extended Canadian Middle Atmosphere Model: Zonal-mean climatology and physical parameterizations

V. I. Fomichev,[1] W. E. Ward,[2] S. R. Beagley,[1] C. McLandress,[3] J. C. McConnell,[1] N. A. McFarlane,[4] and T. G. Shepherd[3]

Received 3 February 2000; revised 18 October 2001; accepted 20 October 2001; published 22 May 2002.

[1] This paper describes the energetics and zonal-mean state of the upward extension of the Canadian Middle Atmosphere Model, which extends from the ground to ~210 km. The model includes realistic parameterizations of the major physical processes from the ground up to the lower thermosphere and exhibits a broad spectrum of geophysical variability. The rationale for the extended model is to examine the nature of the physical and dynamical processes in the mesosphere/lower thermosphere (MLT) region without the artificial effects of an imposed sponge layer which can modify the circulation in an unrealistic manner. The zonal-mean distributions of temperature and zonal wind are found to be in reasonable agreement with observations in most parts of the model domain below ~150 km. Analysis of the global-average energy and momentum budgets reveals a balance between solar extreme ultraviolet heating and molecular diffusion and a thermally direct viscous meridional circulation above 130 km, with the viscosity coming from molecular diffusion and ion drag. Below 70 km, radiative equilibrium prevails in the global mean. In the MLT region between ~70 and 120 km, many processes contribute to the global energy budget. At solstice, there is a thermally indirect meridional circulation driven mainly by parameterized nonorographic gravity-wave drag. This circulation provides a net global cooling of up to 25 K d^{-1}. *INDEX TERMS:* 0342 Atmospheric Composition and Structure: Middle atmosphere—energy deposition; 3337 Meteorology and Atmospheric Dynamics: Numerical modeling and data assimilation; 3334 Meteorology and Atmospheric Dynamics: Middle atmosphere dynamics (0341, 0342); *KEYWORDS:* middle atmospheric, mesosphere and lower thermosphere, general circulation model, parameterizations, energy budget

1. Introduction

[2] Over the past decade, the mesosphere/lower thermosphere (MLT) region (~70 to 120 km) has become the object of intense research interest. Several instruments on board the Upper Atmosphere Research Satellite (UARS), such as the Wind Imaging Interferometer (WINDII) [*Shepherd et al.*, 1993] and the High-Resolution Doppler Imager (HRDI) [*Hays et al.*, 1993], have investigated the wind and temperature structure of this region. Important measurements have also been made by the Cryogenic Infrared Spectrometers and Telescopes for the Atmosphere (CRISTA) experiment [*Riese et al.*, 1999] on two shuttle missions and will be made by the upcoming Thermosphere-Ionosphere-Mesosphere Energetics and Dynamics (TIMED) satellite. These observations have provided (or will provide) a unique set of information on the MLT region. However, since our understanding of atmospheric processes is primarily tested by our ability to simulate these processes from first principles, the development of first principles numerical models, and their evaluation against measurements, is vitally important.

[3] The MLT region has tended to be a dividing line for modelling efforts, with thermospheric models having this region as their lower boundary [e.g., *Fuller-Rowell and Rees*, 1980; *Dickinson et al.*, 1984], and middle atmosphere general circulation models (GCMs) having the MLT region as their upper boundary [*Pawson et al.*, 2000]. The reason for this is the differing dynamical regimes in these two regions. The thermosphere is primarily a system driven by external (solar) influences, where molecular viscosity is large enough that the associated time scales are short, on the order of a day. This means that to a first approximation the thermosphere can be treated in isolation. In contrast, below the mesopause where the effects of viscosity are weak and timescales are long, the region is characterized by a much higher degree of internal variability. This means that it is necessary to represent the region from the ground up to capture the dynamical forcing from the more massive troposphere.

[4] Being a transition zone between the stratosphere and thermosphere, the MLT region is of interest in its own right. This is a region where upward propagating disturbances from the lower atmosphere, such as gravity waves and tides, reach their maximum amplitudes and break, depositing momentum and energy into the large-scale flow. This is also a region where signals of global atmospheric change, such as the effects of increases in CO_2, are significantly greater than in the troposphere and stratosphere [e.g., *Berger and Dameris*, 1993; *Akmaev and Fomichev*, 1998].

[5] Over the past 2 decades a number of numerical models have been developed to explore phenomena in the MLT region. These models can be loosely classified into two groups. The first group consists of models with lower boundaries above the troposphere [e.g., *Akmaev et al.*, 1992; *Chan et al.*, 1994; *Roble and Ridley*, 1994]. The second group consists of models with lower boundaries at the surface, but with the troposphere treated in a simplified way

[1]Earth and Atmospheric Sciences Department, York University, Toronto, Ontario, Canada.
[2]Department of Physics, University of New Brunswick, Fredericton, New Brunswick, Canada.
[3]Department of Physics, University of Toronto, Toronto, Ontario, Canada.
[4]CCCma, Meteorological Service of Canada, Victoria, British Columbia, Canada.

0148-0227/02/2001JD000479$09.00

[e.g., *Berger and Dameris*, 1993]. Although these models are able to reproduce many of the observed features of the MLT region (e.g., cold summer mesopause, tidal motion), they do not represent a broad spectrum of geophysical variability.

[6] In contrast to the models just described, atmospheric GCMs contain self-consistent comprehensive tropospheric physics and, therefore, are potentially much better suited for studying the coupling between the troposphere and the MLT region from first principles. The first GCM extended into the lower thermosphere (up to ~165 km) was the Middle Atmosphere Circulation Model at Kyushu University (MACMKU) [*Miyahara et al.*, 1993]. Among the other GCMs, the Canadian Middle Atmosphere Model (CMAM) [*Beagley et al.*, 1997] and the U.K. Universities' Global Atmospheric Modelling Programme (UGAMP) model [*Norton and Thuburn*, 1997] were the ones having the highest upper boundaries (~95 km).

[7] However, all models with an upper boundary below the turbopause must incorporate an artificial damping layer near the lid to prevent spurious reflections of vertically propagating waves. This is usually accomplished using a Rayleigh-friction sponge layer. While the sponge may not have a significant impact on the propagating diurnal tide at mesospheric heights [*McLandress*, 1997], it can feed back artificially on the zonal-mean circulation in the lower atmosphere if an imposed force, like gravity-wave drag, is applied within or near the sponge layer [*Shepherd et al.*, 1996]. A lid at 95 km then becomes problematical for simulation of the MLT region. By extending the model into the thermosphere, molecular diffusion and ion drag act to dissipate upward propagating waves and thus provide a natural sponge. Such an extension is clearly required for first principles simulation of the MLT region.

[8] Recently, the upper boundary of the UGAMP model has been extended to ~125 km [*Norton and Thuburn*, 1999]. This was done without the inclusion of any new physics in the thermosphere; for example the breakdown of local thermodynamic equilibrium (LTE) conditions for radiative processes was neglected. An updated version of the MACMKU [*Miyahara and Miyoshi*, 1997] has included more realistic upper atmosphere physics, but neglects extreme ultraviolet (EUV) heating, has relatively coarse vertical resolution in the troposphere, and uses Rayleigh friction as a replacement for a gravity-wave drag parameterization.

[9] *Beagley et al.* [2000] presented the first results from an extended version of the CMAM. In contrast to the extended UGAMP model, the extended CMAM has a higher lid and includes new parameterized physical processes of importance in the lower thermosphere. The simulation carried out with the extended CMAM showed good agreement with UARS observations of both the zonal-mean zonal wind and tides in the MLT region. In particular, the model reproduced the zonal-mean jet reversals in the upper mesosphere, and realistic diurnal and semidiurnal tides below 120 km, including the semiannual variation of the amplitude of the propagating diurnal tide in the mesosphere. Development of the model has continued, and in its present form the model now includes parameterized physical processes of importance in the lower thermosphere such as solar heating due to absorption by O_3 and O_2 at wavelengths shorter than 0.25 μm and by O_2, N_2 and O in the EUV region, a modified non-LTE parameterization for the 15-μm CO_2 band, chemical heating due to atomic oxygen recombination, molecular diffusion and viscosity, ion drag, and the effects of momentum and energy deposition by unresolved nonorographic gravity waves together with the inclusion of eddy diffusion generated by gravity-wave breaking. The extended model has been developed to improve the simulation of the standard CMAM (i.e., 95-km lid) in the MLT region and does not yet include such thermospheric processes as Joule heating and the heating associated with electromagnetic processes in polar regions.

[10] This paper provides a detailed description of the extended CMAM, with special attention paid to the new physical parameterizations and their effects on the energy and momentum balances of the MLT region. The outline of the paper is as follows: section 2 presents a general description of the model and the climate simulation, section 3 describes the new physical parameterizations, section 4 presents the zonal-mean climatology produced by the model, section 5 examines the relative importance of the various terms in the energy and momentum equations, and section 6 summarizes the main results. In the appendix details are given concerning the treatment of the horizontal diffusion and time filter in the extended model.

2. General Description of the Model and the Simulation

[11] The standard version of the CMAM is a spectral T32 GCM of the troposphere and middle atmosphere which has its upper boundary at 6×10^{-4} mbar (~95 km). That version has 50 vertical layers, of which 17 are in the troposphere, with a vertical resolution ranging from ~150 m near the surface to ~2 km near the tropopause and tending to a roughly constant value of ~3 km in the region above. The T32 configuration provides a latitudinal-longitudinal resolution of ~6° × 6° A full description of the first generation CMAM is given by *Beagley et al.* [1997]. The model also has an option for inclusion of interactive chemistry and has been successfully used to study ozone climatology [*de Grandpré et al.*, 2000].

[12] To develop the extended version of the model, the upper boundary has been raised to 2×10^{-7} mbar (geopotential height ~210 km) by adding 20 new layers which are equally spaced in pressure scale height with a constant step of ~0.4. New physical parameterizations relevant to the MLT region and to the thermosphere have been implemented. These are (1) an updated version of the non-LTE parameterization for the 15-μm CO_2 band; (2) solar heating due to absorption by O_2 in the Schumann-Runge bands and continuum, and by O_2, N_2 and O in the EUV spectral region; (3) parameterized chemical heating; (4) molecular diffusion and viscosity; (5) ion drag; and (6) a modified nonorographic gravity-wave drag (GWD) scheme. A more detailed description of these parameterizations is given in section 3.

[13] In order to avoid an excessively short time step, a height-dependence was included in the time filter and the horizontal diffusion was increased in the thermosphere. This permits a 5-min time step to be used, which makes long integrations feasible. The necessary modifications to the diffusion and time filter are discussed in detail in Appendix A.

[14] The model does not include ionospheric processes such as geomagnetic effects and uses prescribed distributions for atmospheric constituents. The latitude-altitude ozone distribution was taken from *Wilcox and Belmont* [1977], and globally averaged vertical profiles for O_2, N_2 and O were taken from the Mass Spectrometer and Incoherent Scatter (MSIS) 90 model [*Hedin*, 1991]. The vertical profile for CO_2 corresponds to the 360 ppm CO_2 model from *Fomichev et al.* [1998]: CO_2 volume mixing ratio remains constant up to ~85 km and decreases rapidly in the thermosphere.

[15] The CMAM assumes a complete conversion of kinetic energy losses into heat. This conversion is applied to the orographic GWD, ion drag, and molecular viscosity. Note that it is not applied to nonorographic GWD since the parameterization produces its own heating term nor to the horizontal diffusion of vorticity and divergence since the associated heating is negligible.

[16] After implementation of the major physical parameterizations (EUV heating, molecular diffusion and viscosity, non-LTE, and GWD schemes), the model was spun up starting from initial conditions generated by an existing CMAM output below 95 km

and, for simplicity, height-independent values for temperature and wind in the region above. The spin up was carried out using strong mechanical damping and a short 1-mine time step. The model was then integrated for 7 years with some minor modifications of the physical processes being made to the initial setup. In its present configuration the model has been run for 3 years, and results for the last year are presented.

3. Physical Parameterizations

[17] To adequately represent processes in the MLT region, the model should include parameterizations of the physical processes most important in the region. In this section the physical parameterizations implemented in the extended version of the CMAM are described.

3.1. Radiative Scheme and Chemical Heating

[18] The radiative scheme consists of the one used in the standard version of the CMAM (described in the work of *Beagley et al.* [1997] and *McFarlane et al.* [1992]), as well as some additional modules for the treatment of radiative transfer in the MLT region. The updated scheme includes heating due to absorption of solar energy in the spectral interval from the EUV to the near infrared region, and infrared cooling in the most important spectral bands, with account being taken of non-LTE processes in the MLT region. In the stratosphere and below the radiative transfer processes account for clouds, aerosols, and Rayleigh scattering.

3.1.1. Solar heating. [19] The original CMAM solar radiation scheme uses the parameterization of *Fouquart and Bonnel* [1980] and accounts for absorption by O_3, H_2O, CO_2, and O_2 at wavelengths longer than 0.25 μm. For use in the middle atmosphere, solar heating due to absorption by O_3 at wavelengths shorter than 0.25 μm and by O_2 in the Schumann-Runge bands and continuum was added using the parameterization of *Strobel* [1978].

[20] To calculate the solar heating above ~65 km, one has to account for energy losses which occur upon absorption of solar radiation that result in deviations from unit heating efficiency.This occurs because the atmospheric density in this region becomes so low and the collisions between molecules so infrequent that the energy of the excited products of photolysis can be partly emitted before being quenched by collisions (i.e., thermalized). For the O_3 Hartley band and O_2 Schumann-Runge continuum this variation in heating efficiency is associated with energy losses of such excited photolysis products as $O_2(^1\Delta)$ and $O(^1D)$ through direct emissions in the 1.27-μm O_2 band and 630-nm O line or through collisional transfer followed by emission in the 762-nm O_2 line or the 4.3- and 15- μm CO_2 bands [*Fomichev and Shved*, 1988; *Mlynczak and Solomon*, 1993]. These processes result in losses of up to 30 and 17% of the total energy absorbed in the O_3 Hartley band and O_2 Schumann-Runge continuum, respectively. To account for this effect the approach suggested by *Mlynczak and Solomon* [1993] was used.

[21] At thermospheric heights, solar heating mostly results from the absorption of EUV radiation by O_2, N_2, and O, followed by photoionization. To calculate the EUV heating, absorption in 37 spectral intervals of 5-nm width in the range between 5 and 105 nm has been taken into account. Solar fluxes and absorption coefficients for each spectral interval and each constituent were calculated from the EUV model by *Richards et al.* [1994], assuming moderate solar activity (index F_{107} equal to 150). Unfortunately, no simple approach exists for the calculation of the EUV heating efficiency; in order to estimate which part of the photoionization energy is converted into heat, such a calculation should involve consideration of the thermospheric chemistry. To avoid this complication, we have instead used the constant value of 36.6% for the EUV heating efficiency as recommended by *Roble* [1995].

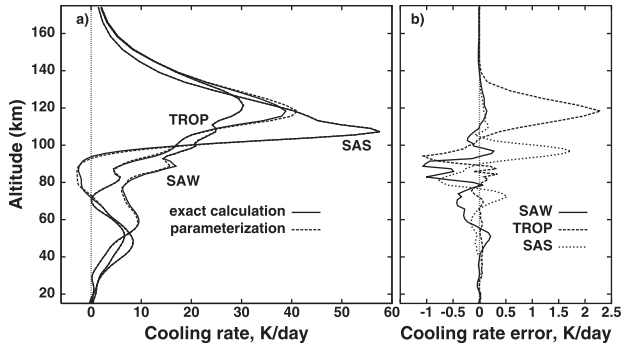

Figure 1. (a) Cooling rates and (b) cooling rate errors from the parameterization for the 15-μm CO_2 band: exact calculation, reference calculation by *Ogibalov et al.* [2000]; parameterization, modified version of the *Fomichev et al.* [1998] parameterization. The three profiles shown are for sub-Arctic winter (SAW), sub-Arctic summer (SAS), and tropics (TROP).

[22] In the extended CMAM, atmospheric sphericity is taken into account in the solar heating calculations. This results in heating for solar zenith angles of up to 100° and 104.5° at 100 and 210 km, respectively,thus providing a more realistic day-night transition.

3.1.2. Infrared cooling. [23] The CMAM infrared radiative scheme consists of two modules. Below ~30 mbar (24 km), infrared cooling due to H_2O, CO_2, O_3, CH_4, N_2O, CFC11, and CFC12 is taken into account using the method developed by *Morcrette* [1991]. Above ~8 mbar (33 km), a matrix parameterization for the 9.6-μm O_3 band (taken from *Fomichev and Blanchet* [1995]) and a modified matrix parameterization for the 15-μm CO_2 band [*Fomichev et al.*, 1998] are used. The latter two parameterizations provide an accurate and computationally efficient calculation of radiative cooling in the middle and upper atmosphere. Between 30 and 8 mbar, the *Morcrette* [1991] and middle/upper atmosphere schemes are merged using linear interpolation between the infrared cooling rates provided by the two schemes (see discussion by *Fomichev and Blanchet* [1995]).

[24] To allow for the more frequent calculation of the infrared cooling in the MLT region (where temperature perturbations are large and radiative time scales are short), while maintaining computational efficiency, the two schemes are decoupled. This permits the computationally intensive *Morcrette* [1991] scheme to be calculated every 6 hours, as in the standard version of the CMAM, and the computationally efficient matrix parameterizations of *Fomichev et al.* [1998] and *Fomichev and Blanchet* [1995] to be calculated every time step. In addition to the increased numerical stability of the model in the MLT, this approach also results in some heating above ~90 km. The reason for this is that overly long radiative time steps do not adequately represent the fast radiative damping that exists in the MLT region, which leads to spurious temperature variability and a cold bias from the resulting cooling. Such sensitivity underscores the importance of reevaluating the implementation of physical parameterizations when extending a climate model into the lower thermosphere, where timescales are generally much shorter than they are lower down.

[25] To be valid in and above the mesopause region, it is crucial for an infrared scheme to include the treatment of the breakdown of local thermodynamic equilibrium (LTE) conditions. The parameterization for the 15-μm CO_2 band used in the CMAM [*Fomichev et al.*, 1998], which includes non-LTE effects, has recently been modified in the non-LTE region to better match the new reference cooling rates from *Ogibalov et al.* [2000]. Figure 1 shows a comparison between the 15-μm

CO_2 band cooling calculated using the updated parameterization and the reference calculations, using the same input data as in *Fomichev et al.* [1998] for three "extreme" vertical profiles of temperature. The updated parameterization is seen to provide a good approximation to the cooling rates throughout the middle and upper atmosphere. Above 100 km, the difference between the parameterization and reference calculations is less than 2.4 K d^{-1}, or 5%. In the region between 80 and 90 km the maximum error is 1 K d^{-1}, and between 90 and 100 km it is 1.7 K d^{-1}. This is in contrast with the 1.5 and 3.5 K d^{-1} differences, respectively, that existed before the modification to the scheme.

[26] One of the most important factors determining the value of the 15-μm CO_2 band cooling in the lower thermosphere is the quenching rate constant for collisions between CO_2 and O. In the current model simulations we use a value of 3×10^{-18} m^3/s. This value appears to represent the best fit between available measurements of the constant, as discussed by *Fomichev et al.* [1998], and is also supported by numerical simulations of the atmospheres of Venus, Earth, and Mars [*Bougher et al.*, 1994].

[27] At thermospheric heights, radiative cooling in the 5.3-μm NO band, which peaks at ~140–150 km [*Kockarts*, 1980], is also of importance. This mechanism is not explicitly calculated in the present version of the model, although the associated radiative losses of energy are accounted for through the solar EUV heating efficiency [*Roble*, 1995], as discussed above.

3.1.3. Chemical heating. [28] Chemical heating is another significant source of energy in the MLT region [e.g., *Mlynczak and Solomon*, 1993]. A proper treatment of chemical heating in the model requires an interactive chemistry scheme and a consideration of the different channels for converting chemical potential energy into heat. Since the extended CMAM does not at present include interactive chemistry, only the effect of the recombination reaction $O + O + M \rightarrow O_2 + M$ has been taken into account. This source of heat is mainly related to the absorption of solar energy in the thermosphere,where part of the absorbed energy is transformed into chemical potential energy that is transported down to the MLT region. To be consistent with the solar and non-LTE infrared schemes, the globally averaged vertical profiles of atomic oxygen, O_2 and total air number density from the MSIS-90 model of *Hedin* [1991] have been used in our simplified chemical heating calculation. Use of these fixed globally averaged profiles means that spatial and temporal variations in chemical heating can only arise from variations in the atmospheric density and from the temperature dependence of the recombination reaction rate constant.

3.2. Molecular Diffusion and Viscosity

[29] Thermal molecular diffusion in the vertical plays a crucial role in the energy balance of the thermosphere, providing a major sink of energy in this region. Since we are primarily interested in the region of the atmosphere below 130 km, simplified forms for the diffusion coefficients have been adopted, as is standard practice [*Roble et al.*, 1987]. The temperature (T) dependence of the coefficients of viscosity (ν) and thermal conductivity (η) are taken to be proportional to $T^{0.69}$, as given by the empirical formula in the work of *Banks and Kockarts* [1973]. For ν in units of kg m^{-1} s^{-1} the coefficient of proportionality is set to its value at 120 km using the model atmosphere provided in *Banks and Kockarts* [1973], namely 3.563×10^{-7}, so that $\nu = 3.563 \times 10^{-7} T^{0.69}$. As described by *Richmond* [1991], the coefficient of thermal conductivity may be approximated throughout the thermosphere as $\eta = C c_p \nu$ where c_p is the heat capacity at constant pressure. Here we set C to 1.4, its value at 120 km.

[30] Above ~90 km, thermal molecular diffusion starts to dominate over eddy heat diffusion which is mainly generated by the unresolved breaking gravity waves and will be discussed later. The globally averaged thermal molecular diffusion coefficient increases exponentially with height from ~10 m^2/s at 90 km up to ~10^6 m^2/s at 210 km, whereas the thermal eddy diffusion coefficient peaks at ~80 km with a value of 10–20 m^2/s.

[31] When choosing the height for the upper boundary of the model, some care must be taken to ensure that the thermal balance in that region is not too complex. Initial attempts to run the model with a lid near 150 km failed because the simple (zero flux) boundary condition used for the thermal diffusion did not approximate the thermal balance conditions at this height. When the upper boundary was raised to ~210 km, where EUV heating and thermal diffusion provide the dominant energy balance, this boundary condition proved adequate. The upper boundary condition implemented in the present version of the model accounts for the energy balance above the lid: the heat flux by thermal diffusion at the upper boundary is set equal to the extinction of the EUV flux occurring above the model lid. This boundary condition is more physically based than the simple zero-flux approach, although the model response to the more sophisticated upper boundary condition is rather small.

3.3. Ion Drag

[32] Momentum exchange between the ionized and neutral gases is taken into account using the ion drag parameterization described by *Hong and Lindzen* [1976]. Since ions tend to move along magnetic field lines in the E region, neutral molecules moving across the field lines are decelerated. The zonal and meridional ion drag coefficients (k_u and k_v) are given as

$$k_{u=}\nu(z) \tag{1}$$

$$k_v = \nu(z)\sin^2 I, \tag{2}$$

where ν (which is composed of the Pederson electrical conductivity, the magnitude of the Earth's magnetic field and the neutral gas density) is the altitude-dependent coefficient taken from Figure 4 of *Hong and Lindzen* [1976] for minimum solar activity. I is the dip angle of the magnetic field lines which, assuming coincidence of the Earth's magnetic and geographic poles, is given by

$$\tan(I) = -2\tan(\theta), \tag{3}$$

where θ is geographic latitude. In the present version of the model, for the purpose of simplicity, we have neglected the Lorentz deflection terms since the Hall electrical conductivity decreases rapidly above its peak at ~130 km. Although its magnitude is similar to that of the Pederson conductivity below 130 km, its effect will be found in a narrow height region near ~130 km, which is at the upper edge of the main region of interest. This approach has also been taken in thermospheric tidal studies such as *Hong and Lindzen* [1976] and *Forbes and Garrett* [1976]. Ion drag is implemented in the extended CMAM using an implicit time formulation. The coefficient ν is interpolated to pressure levels using the geopotential.

3.4. Gravity-Wave Parameterization

[33] The effects of both unresolved orographic and nonorographic gravity waves are included in the extended version of the CMAM. The former are treated using the parameterization of *McFarlane* [1987], which is a standard component of the tropospheric GCM [*McFarlane et al.*, 1992] from which the CMAM was built. The nonorographic gravity waves are treated using the Doppler spread parameterization (DSP) of *Hines* [1997a, 1997b]. Owing to both the complexity of wave-breaking processes and the lack of global observations of the spatial and temporal spectra of gravity-wave momentum fluxes in the troposphere needed to

constrain the parameterization, it is fair to say that the nonorographic scheme is the least understood and therefore most uncertain of the parameterizations discussed here.

[34] A detailed discussion of the DSP and its implementation and impact in the standard CMAM is given by *McLandress* [1998]. Several modifications to the scheme have subsequently been made. These comprise a correction to the equation governing the rate of energy deposition [*Hines*, 1999] and the inclusion of the eddy diffusion and gravity-wave heating terms. The settings of the tunable parameters (the so-called "fudge" factors) are the following: $\Phi_1 = 1.5$, $\Phi_2 = 0.3$, $\Phi_3 = 1.0$, $\Phi_5 = 1.0$, and $\Phi_6 = 0.25$ (Note Φ_4 is not needed since the model is hydrostatic). The gravity-wave source is specified to be at the Earth's surface where, for simplicity, the horizontal wind vertical wave number (m) spectrum is taken to be proportional to m, and the RMS horizontal wind is set to 1 m s^{-1}. To prevent excessively large values of momentum deposition in the thermosphere a maximum allowable vertical wavelength of $\sim$19 km is included in the source spectrum. The typical horizontal wave number is set to 1.4×10^{-5} m^{-1}. Eight horizontal azimuths are employed. Instead of using the molecular viscosity to compute the cutoff wave number at thermospheric heights as suggested by *Hines* [1997a, 1997b], a simpler approach of exponentially smoothing the drag, diffusion coefficients and heating rates to zero above 105 km has been employed. This difference has a negligible effect on the MLT region.

[35] The initial simulations presented by *Beagley et al.* [2000] used the original (and incorrect) formulation of the eddy diffusion coefficient given by *Hines* [1997a] and did not include the gravity-wave (GW) heating term. When the corrected form was implemented an excessively cold summer mesopause occurred. At this point we used the same diffusion coefficients for both momentum and heat, which is equivalent to a turbulent Prandtl number of one. However, there are strong reasons to believe that the turbulent Prandtl number in this region should be significantly greater than unity [*McIntyre*, 1989]. In the present simulation a value of three was introduced, which reduces the eddy heat diffusion by that amount and produces, together with the GW heating term, more reasonable summer mesopause temperatures. The same approach is used by *Akmaev* [2001] in his implementation of the DSP.

4. Zonal-Mean Climatology

[36] The first step in model validation is a comparison of the simulated zonal-mean climatology with the observations. In this section, the model temperature and wind fields are presented and compared to the MSIS-90 model [*Hedin*, 1991] and the UARS wind observations [*McLandress et al.*, 1996]. Since the extended CMAM does not include geomagnetic effects or ion and neutral chemistry (which is needed for the calculation of the EUV heating efficiency), results are shown only up to 150 km. To convert the results to approximate geometric altitude, the CMAM data were interpolated from pressure to altitude surfaces using the global average geopotential.

4.1. Temperature Field

[37] Figure 2 shows the globally averaged temperature profiles for June for the extended and standard versions of the CMAM, as well as the MSIS-90 model [*Hedin*, 1991]. The temperature profile produced by the extended model is similar to that of the standard version up to $\sim$90 km. Near the upper boundary, the latter does not reproduce the temperature minimum at the mesopause and is colder than the extended model by $\sim$15K. This temperature bias appears to be associated with the location of the model lid at 95 km. It will be seen later that the thermally indirect wave-driven circulation leads to a net dynamical cooling in the lower thermosphere; in the standard CMAM, where the wave drag is constrained to occur at lower altitudes, this cooling region moves down.

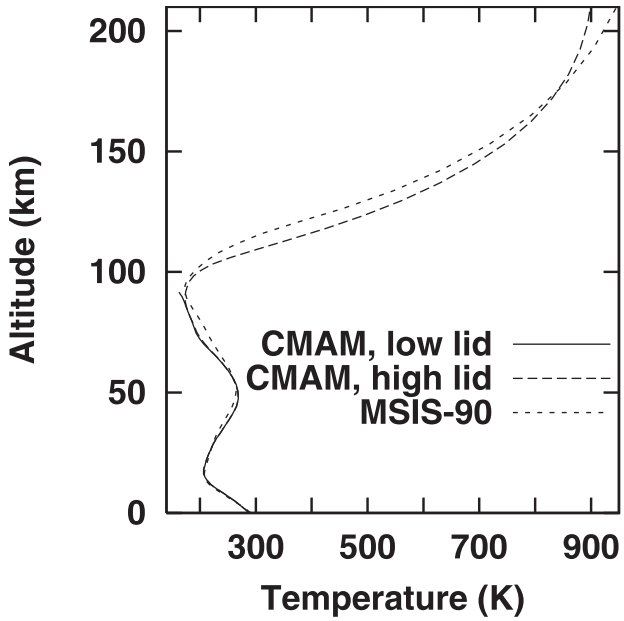

Figure 2. Globally averaged temperature profiles: CMAM, low lid, profile obtained from the standard CMAM (i.e., with a lid at $\sim$95 km) using the same physical parameterizations as in the extended CMAM but with the inclusion of nonzonal Rayleigh-friction sponge in the top model layer; CMAM, high lid, profile obtained using the extended CMAM; MSIS-90, temperature profile from the MSIS-90 model [*Hedin*, 1991].

[38] At thermospheric heights the temperature profile from the (extended) CMAM is in good agreement with the MSIS-90 model [*Hedin*, 1991] but is somewhat higher below $\sim$170 km and somewhat lower above (Figure 2). This disagreement is attributable to deficiencies in both the CMAM and the MSIS-90 model. It should be reiterated here that since we are mostly interested in processes occurring below $\sim$120 km, the CMAM does not include some important thermospheric processes, which would be of importance in the upper part of the model domain. Moreover, there are some uncertainties in the CO_2-O quenching rate constant needed for the calculation of the infrared cooling, and in the efficiency of the EUV solar heating. Such uncertainties are usually resolved by tuning the model results, which we have not done, using instead the values recommended in the literature for these parameters.

[39] The zonally averaged temperature fields for June and March from the CMAM, together with those from the MSIS-90 model [*Hedin*, 1991], are shown in Figure 3. As can be seen, there is good agreement between the two throughout the entire domain. The model reproduces the latitudinal temperature gradients quite well: there is a cold tropical tropopause in both seasons, a cold winter lower stratosphere, an elevated winter stratopause, a warm summer stratopause, and a cold summer mesopause. Temperature increases rapidly in the thermosphere, reaching $\sim$700K near 150 km.

4.2. Zonal Wind Field

[40] A comparison between the daytime-mean zonal wind from the CMAM and that from the WINDII and HRDI instruments on the UARS satellite is shown in Figure 4. The latter results are similar to those shown in the work of *McLandress et al.* [1996]. The observations cover a two-year period starting in February 1992. The WINDII data provide daytime coverage between 90 and 200 km (the nighttime WINDII data that extends only up to 110 km has been excluded from this climatology); the HRDI data are

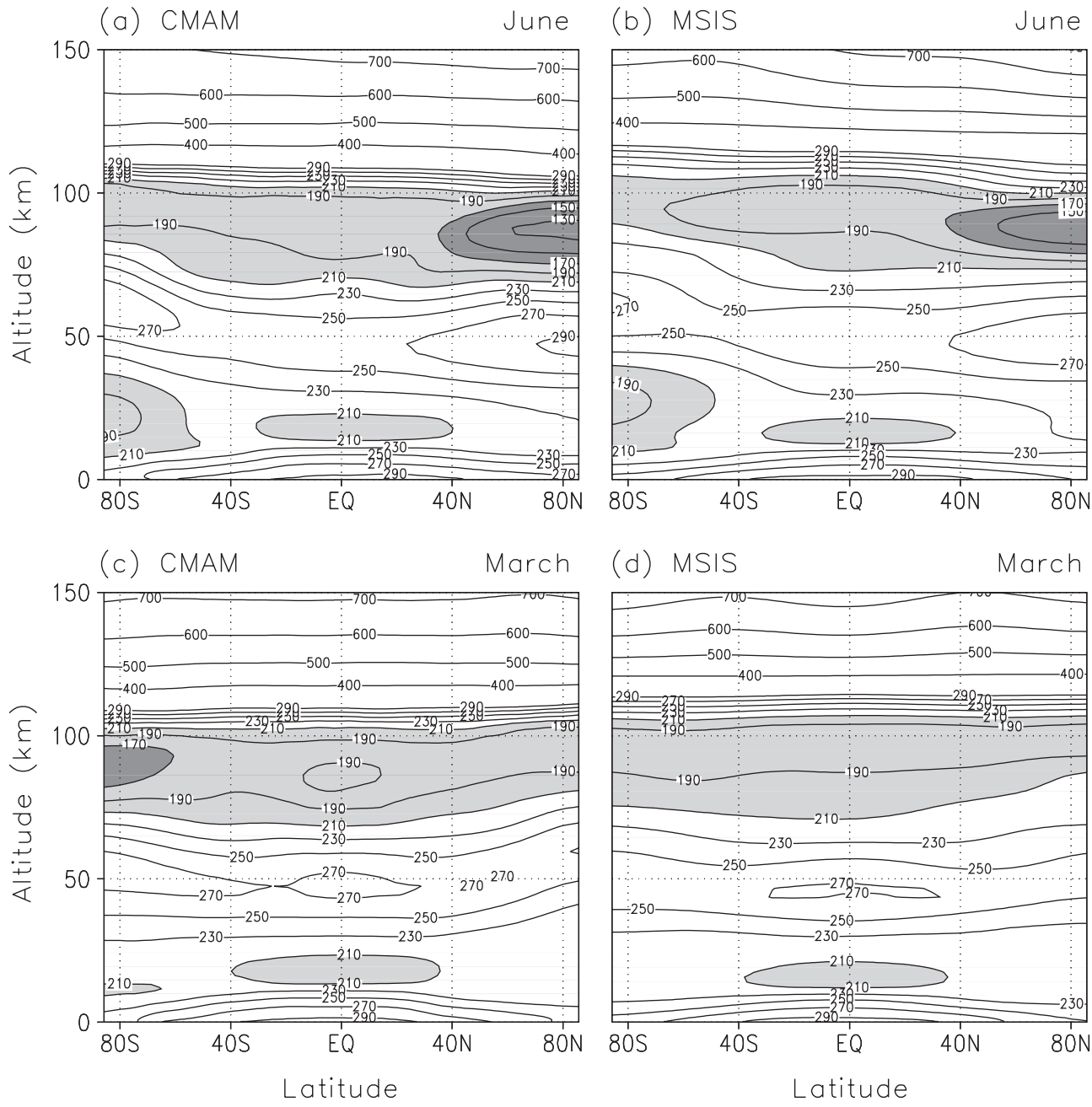

Figure 3. Altitude-latitude temperature (K) distribution simulated by the extended CMAM and obtained from the MSIS-90 model [*Hedin*, 1991]: (a) CMAM, June; (b) MSIS, June; (c) CMAM, March; and (d) MSIS, March.

only for daytime and cover the altitudes from 60 to 110 km. The combined data set was generated by zonally averaging each day of data and binning the results in equally spaced intervals of local solar time, latitude and height. The model daytime-mean is computed as in the work by *Beagley et al.* [2000] by first decomposing the 3 hourly output data into the monthly zonal average and migrating diurnal tide components and then averaging the sum of those two terms over one-half of a day centered at 12 hours local solar time.

[41] The comparison shown in Figure 4 indicates reasonable agreement between the model results and observations. The lower mesosphere is characterized by summer easterlies (westward zonal wind) and winter westerlies (eastward zonal wind). The winds then change direction between 90 and 110 km and revert back to summer easterlies and winter westerlies above 120 km. The zonal wind during equinox is much weaker, but the pattern is more complicated since the zonal wind changes its direction with height several times. The oscillatory pattern seen at low latitudes in the MLT region in March is due in part to the presence of the diurnal tide which is not completely averaged out and which is considerably stronger in equinox than in solstice [e.g., *McLandress*, 1997; *Beagley et al.*, 2000].

[42] The flow reversal seen in the model over the summer mesopause is a direct consequence of the deposition of momentum by the parameterized nonorographic gravity waves. The mesospheric westerlies in the current version of the model are considerably weaker than those shown by *Beagley et al.* [2000], and in fact are in better agreement with the observations. The stronger mesospheric westerlies in the work of *Beagley et al.* [2000] were

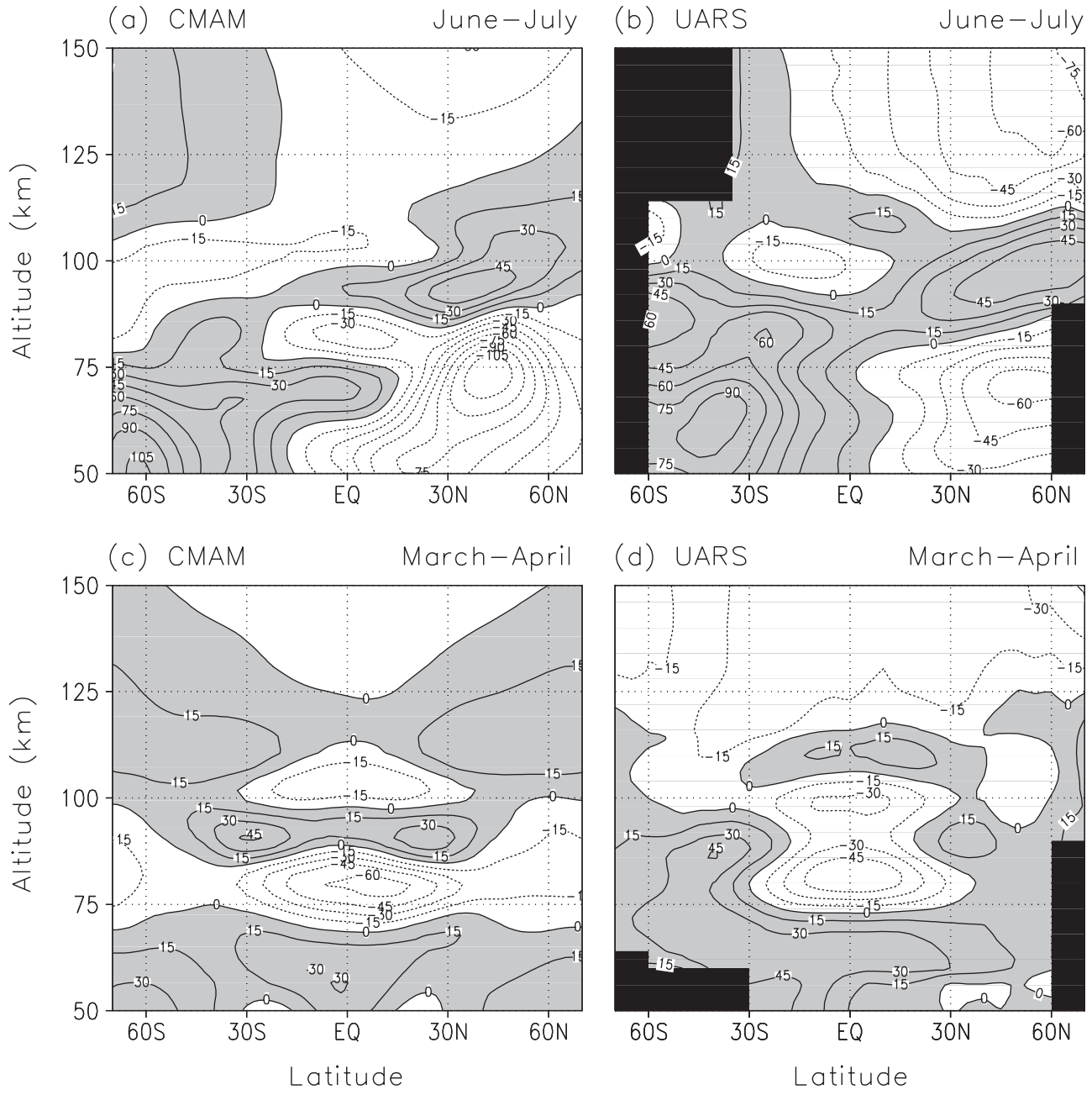

Figure 4. Daytime-mean zonal wind (m s^{-1}) simulated by the extended CMAM and observed by the UARS [*McLandress et al.*, 1996]: (a) CMAM, averaged June and July; (b) UARS, averaged June and July; (c) CMAM, averaged March and April; and (d) UARS, averaged March and April. Regions of the eastward zonal wind (westerlies) are shaded.

the result of weaker GW induced eddy diffusion employed in the earlier version of the model.

5. Physical Processes in the Model

[43] In this section the effects on the model energy and momentum balances of the physical parameterizations described in section 3 are presented, and the relative roles of the different physical processes in the middle and upper atmosphere discussed. Results are shown for June of the last year of the simulation, which is characteristic of the previous years.

5.1. Energy Budget

[44] The constituents of the model energy budget are given by the thermodynamic equation:

$$\frac{\partial T}{\partial t} = -\vec{V}_h \cdot \nabla_h T - \omega\left(\frac{\partial T}{\partial p} - \frac{R^* T}{c_p \mu p}\right) + Q_p, \qquad (4)$$

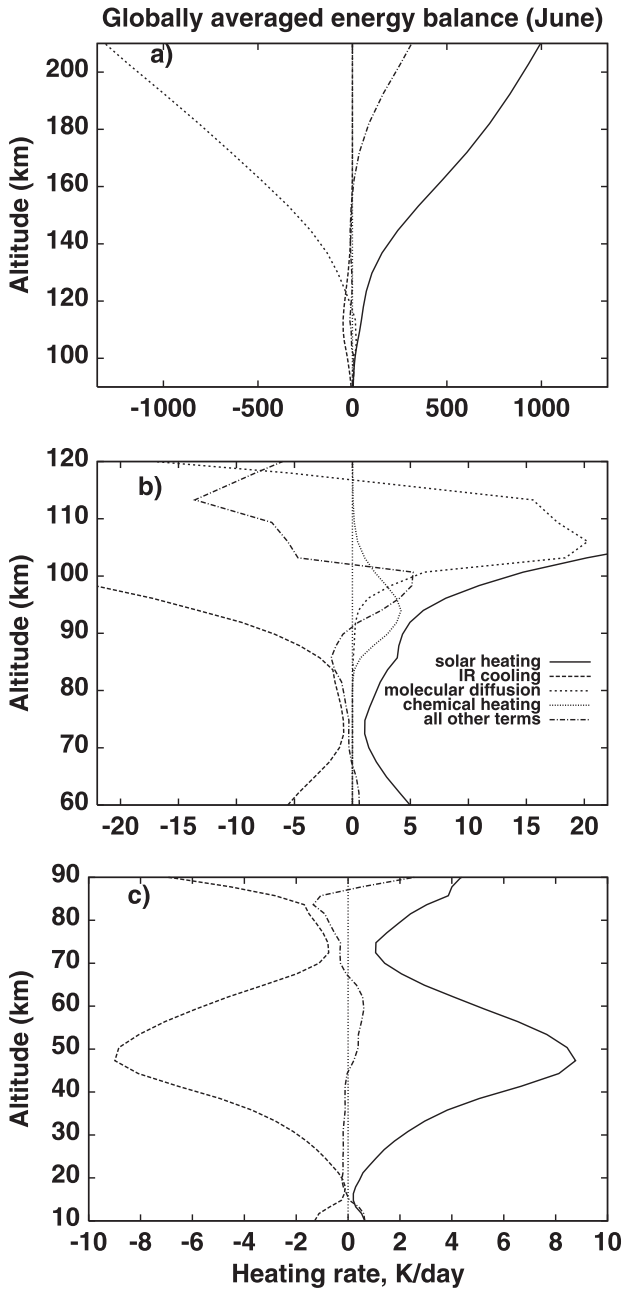

Figure 5. Globally averaged energy balance for June obtained from the extended model in layers (a) 90–210 km, (b) 60–120 km, and (c) 10–90 km: solar heating, contribution provided by absorption of the solar energy; IR cooling, contribution due to infrared radiative transfer; molecular diffusion, effect of thermal molecular vertical diffusion; chemical heating, heating due to recombination reaction $O + O + M \rightarrow O_2 + M$; all other terms, combined effect of all other individual terms.

where ∇_h is the horizontal gradient operator, $\vec{V}_h$ is the horizontal velocity vector, ω is the vertical velocity, R^* is the universal gas constant, c_p is the specific heat at constant pressure, and μ is the molecular weight of air. The first two terms on the right-hand side are the heating rates associated with horizontal and vertical advection, respectively, and include all resolved transport of heat. Note that the vertical advection term includes the adiabatic term. The other term, Q_p, represents the sum of all the parameterized heating terms, namely, solar and chemical heating, infrared cooling, GW heating from the DSP, dissipation of the meridional and zonal winds (i.e., the conversion of kinetic energy losses into heat discussed in section 2), effects of molecular and eddy diffusion, and convective adjustment.

[45] Vertical profiles of the globally and monthly averaged contributions to the energy balance from the different mechanisms are shown in Figures 5 and 6. As can be seen from Figure 5, radiative processes dominate the energy balance throughout the middle and upper atmosphere. There are two regions where the balance is relatively simple. The first lies in the altitude region between the tropopause and ~70 km, where radiative equilibrium occurs. This is consistent with results of *Fomichev and Shved* [1994], who showed that the middle atmosphere is close to radiative equilibrium on a monthly and globally averaged basis. The second region lies above ~130 km in the thermosphere. Here the strong EUV solar heating is primarily balanced by molecular diffusion.

[46] Below ~125 km, solar heating is mostly due to absorption of solar energy by O_3 in the Hartley bands and by O_2 in the Schumann-Runge continuum. This heating maximizes at ~120 km with a value of ~45 K d^{-1}. EUV heating starts to occur at ~100 km and grows rapidly with height while the solar heating due to absorption in other spectral intervals decreases above ~120 km. Below ~125 km, the atmosphere is mainly cooled by the 15-μm CO_2 band. The value of radiative cooling maximizes at ~50 K d^{-1} near 115 km. Cooling due to thermal molecular diffusion starts to dominate above ~125 km.

[47] The pattern is considerably more complicated in the MLT region between 70 and 120 km. Although radiative processes still dominate, other mechanisms are also of importance. A significant contribution to heating, of up to ~20 K d^{-1} near 105 km, is provided by molecular diffusion that transports energy down from the overlying thermosphere and deposits it in this region. Chemical heating also provides a significant contribution of up to ~4 K d^{-1} near the mesopause. The curve labelled "all other terms" in Figure 5 is calculated as a residual after accounting for the time tendency term in equation (4) and can be interpreted as the net dynamical heating. It includes such processes as eddy vertical diffusion, GW heating, conversion of kinetic energy into heat resulting from the dissipation of the horizontal winds, horizontal and vertical advection, and convective adjustment. The vertical structure of this term is similar to the global mean net dynamical

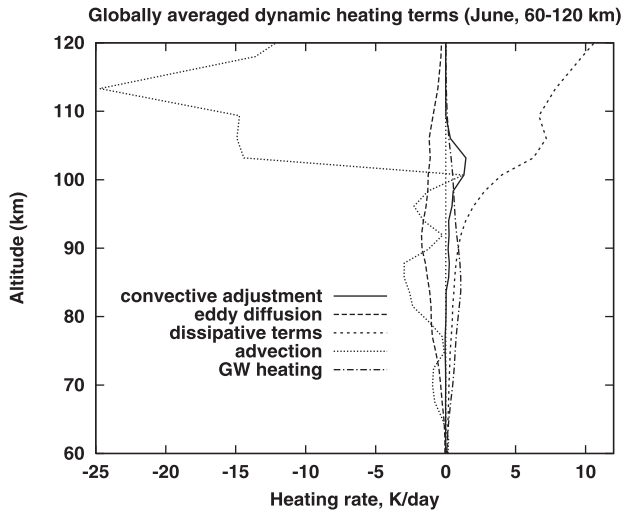

Figure 6. Globally averaged dynamical heating terms in the MLT region: convective adjustment, thermal effect provided by convective adjustment; eddy diffusion, effect of thermal eddy vertical diffusion; dissipative terms, conversion of kinetic energy into heat; advection, thermal effect of the horizontal and vertical advection including adiabatic heating/cooling; GW heating, heating due to breaking gravity waves.

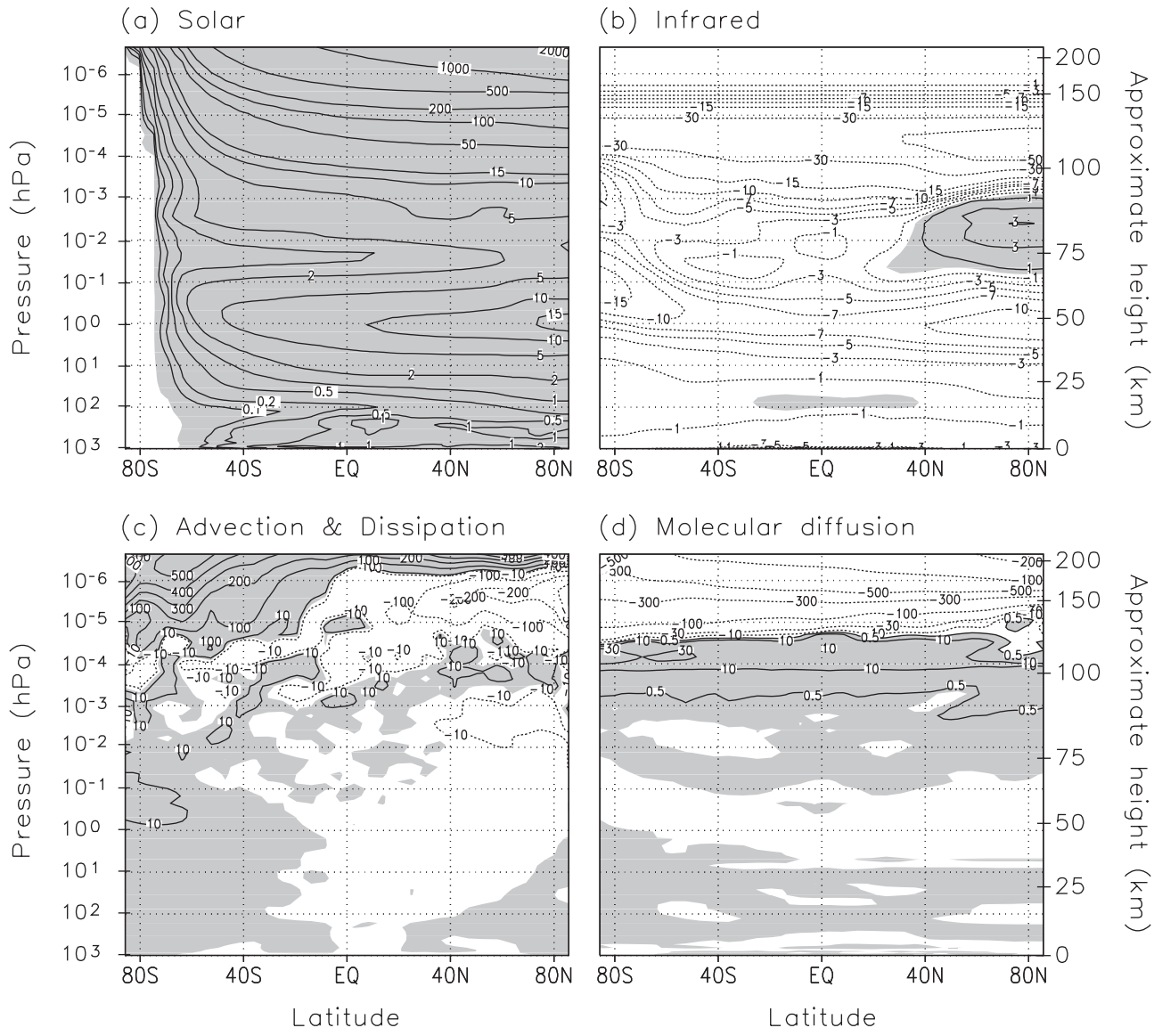

Figure 7. Major energy sources and sinks of the model (K d^{-1}) in June: (a) solar heating, (b) infrared radiative transfer, (c) dynamical heating due to horizontal and vertical advection including adiabatic effects and the conversion of kinetic energy into heat, and (d) contribution by the thermal molecular vertical diffusion. Positive regions are shaded.

heating inferred from the radiative balance by *Fomichev and Shved* [1994].

[48] Vertical profiles of the globally averaged contributions from the dynamical heating terms are shown in Figure 6. These are calculated directly and their sum (not shown) agrees well with the residual in Figure 5. As will be shown later, the dynamical terms play an important role in the polar regions, especially in winter. However even on a globally averaged basis their role in the MLT energy balance is not insignificant. The combined energetic effect of the dynamical terms ("all other terms" in Figure 5b) is cooling below about 90 km (maximum value of ~1.8 K/day at ~85 km), heating between 90 and 105 km (maximum value of ~5 K/day at ~100 km), and cooling again above 105 km (maximum value of ~14 K/day at ~112 km).

[49] The most significant dynamical terms from an energetics point of view are the horizontal and vertical advection terms, and heating due to dissipation of the zonal and meridional winds. The latter grows with height from 4 K d^{-1} near 100 km to 10 K d^{-1} near 120 km (Figure 6). The advective cooling that reaches 25 K d^{-1} near 115 km is due to the thermally indirect wave-driven global-scale circulation with rising air over the cold summer pole. These two mechanisms are also of importance above ~160 km where together they provide up to 25% of the thermospheric heating (Figure 5a). However, in this viscously dominated region the circulation is thermally direct and advection provides a net heating.

[50] The other three dynamical terms (convective adjustment, thermal eddy vertical diffusion, and GW heating) play secondary roles in the globally averaged MLT energetics. Eddy diffusion cools the MLT region at a rate of up to 1.7 K d^{-1} (maximum reached at ~90 km), GW heating maximizes at ~85 km with a value of 1 K d^{-1}, while convective adjustment heats the region around 100 km with a maximum value of 1.4 K d^{-1} (Figure 6). It is also worth noting that the appearance of convection suggests that the model generates statically unstable temperature profiles in the MLT region. This latter point will be discussed in more detail shortly.

[51] The altitude-latitude cross sections of the aforementioned components of the energy balance are shown in Figures 7 and 8.

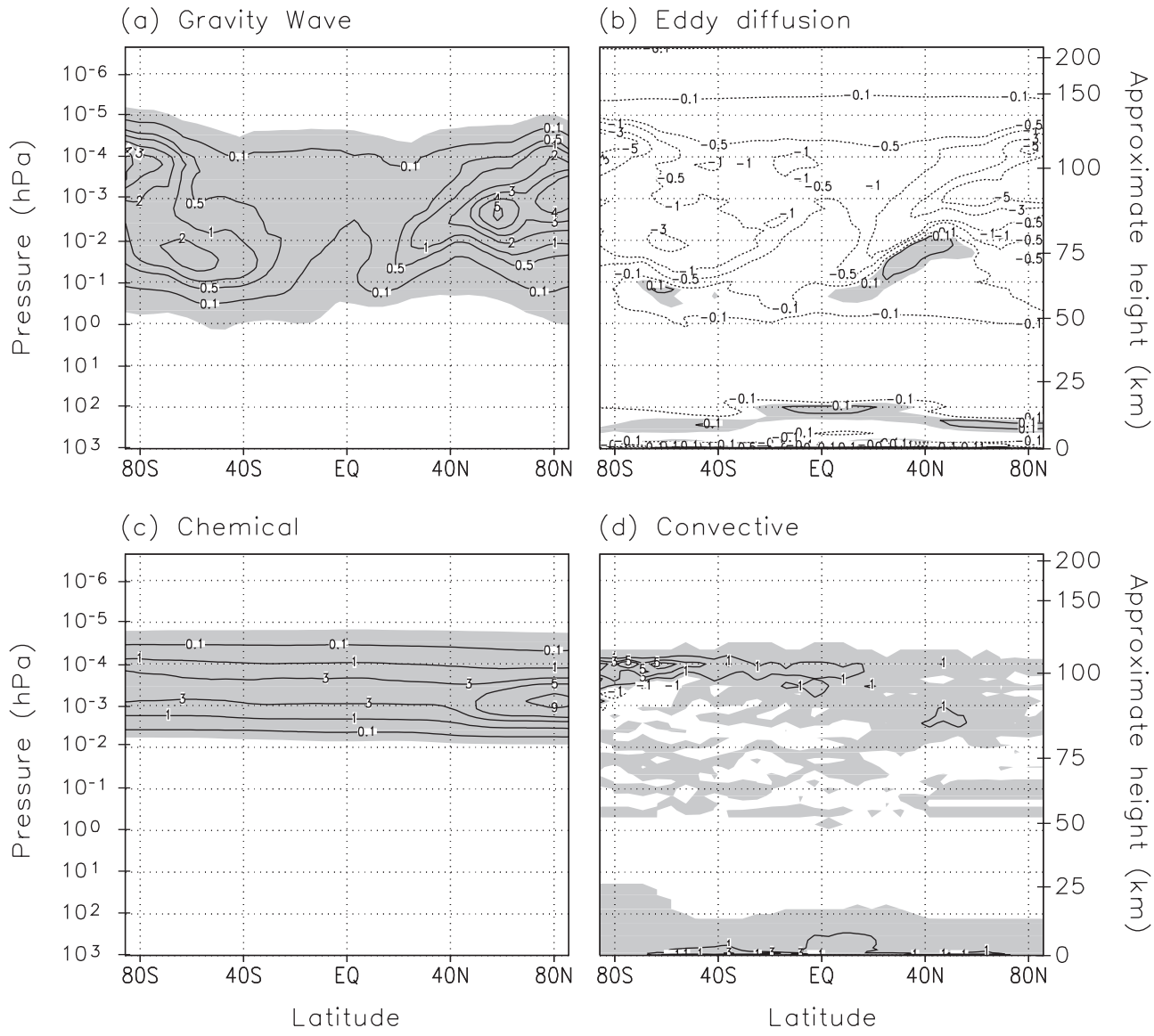

Figure 8. Model energy source and sinks (K d^{-1}) of importance in the MLT region for June: (a) heating due to gravity-wave breaking; (b) thermal eddy vertical diffusion; (c) chemical heating due to the recombination reaction O + O + M → O_2 + M; (d) thermal effects provided by convective adjustment. Positive regions are shaded.

Figure 7 presents contributions of the major energy sources and sinks over the entire model domain, while Figure 8 presents those which are of importance only in the mesopause region.

[52] The major sources of heat in the atmosphere are solar heating (Figure 7a) and dynamical heating associated with both dissipation of the zonal and meridional flow and horizontal and vertical advection (Figure 7c). Note that positive values are shaded. Solar heating exhibits the well-known features of the local maximum near the stratopause provided by O_3 absorption, and the rapid increase with height in the thermosphere due to the absorption of EUV radiation. The maximum solar heating near the stratopause exceeds 15 K d^{-1} over the summer pole. At the top of the model, near the summer pole, solar heating reaches 2000 K d^{-1}. The sphericity effect, which is included in the solar scheme, is explicitly seen in the polar night region where the heating increases with height. The latitudinal structure of the dynamical heating seen in Figure 7c is mostly due to the vertical advection term which has been defined here to include the adiabatic term (see equation (4)). In the absence of solar heating in the polar night near 80° S the atmosphere is heated mainly by this term. In the summer hemisphere the dynamical terms cool the atmosphere, together with infrared cooling (below ~130 km, Figure 7b) and molecular thermal diffusion (above 120 km, Figure 7d).

[53] The infrared cooling (Figure 7b) has two maxima, situated in the stratopause region and near 115 km. There is also a region near the polar summer mesopause where the infrared radiative transfer in fact provides heating (up to ~3 K d^{-1}), not cooling. This effect occurs because of the steep vertical temperature gradient in the cold polar summer mesosphere and the absorption of radiation emitted from the warmer atmosphere below. The contribution from the molecular thermal diffusion (Figure 7d) has a latitudinal and vertical structure which results from the dependence of the diffusion on the second derivative of $T(z)$ together with the temperature dependence of the coefficient of thermal conductivity. Molecular thermal diffusion cools the upper part of the domain by up to 2000 K d^{-1} near the summer pole and by up to 500 K d^{-1} near the winter pole. This energy is transported downward and deposited in the MLT region, resulting in heating of up to 10 K d^{-1} near 105 km at the summer pole and up to 30 K d^{-1} near 110 km at the winter pole.

[54] In the mesopause region, noticeable contributions to the energy balance arise from GW heating, eddy thermal vertical diffusion, chemical heating, and convective adjustment (Figure 8). Chemical heating (Figure 8c) maximizes near the mesopause, with a value of $\sim$4 K d^{-1} and is uniformly distributed with latitude except in the summer polar mesopause region where it reaches 9 K d^{-1}. The latter occurs as a result of the extremely low temperature near the summer polar mesopause and the inverse dependence on temperature of both the recombination reaction rate coefficient and atmospheric density. All other terms shown in Figure 8, namely GW heating (Figure 8a), eddy diffusion (Figure 8b), and convective adjustment (Figure 8d), contribute primarily in the extra tropics. GW heating reaches a maximum of 5 K d^{-1} near the summer pole, while eddy diffusion cools the mesopause region providing maximum values greater than 5 K d^{-1} near both poles.

[55] Convective adjustment contributes up to 5 K d^{-1} heating in a narrow region near 100 km over the winter pole. Because the background temperature is statically stable in this region, the inference is that the convective adjustment reflects the breaking of large amplitude resolved waves in this region. Evidence for significant wave activity is also seen in Figure 10d which shows large values of the Eliassen-Palm flux divergence (EPFD) at this location. Although the origin for these waves is at present uncertain, they are presumed to be disturbances propagating upward from the lower atmosphere. A similar region of convective instability centered at 40 N and $\sim$85 km is associated with enhanced EPFD that results from the instability of the summer mesosphere easterlies (see *Norton and Thuburn* [1999]). The convective heating in the tropics at $\sim$100 km is associated with the diurnal tide as shown by *McLandress* [2002].

[56] The net thermal effect of the parameterized nonorographic gravity waves includes the eddy heat diffusion (which arises primarily from the DSP) and GW heating. In the MLT region this effect can be estimated as the combination of eddy diffusion and GW heating. On a globally averaged basis the sum of these two terms yields a net cooling near the mesopause (Figure 6). However, Figure 9 shows that the net thermal effect of the parameterized gravity waves in the MLT region has a significant latitudinal structure which cancels out to a large extent in the global mean. In the summer hemisphere this effect is positive between $\sim$70 and 88 km (with a maximum of +3 K d^{-1}), and negative above 88 km reaching 4 K d^{-1} cooling near 95 and 105 km. The effect is weaker in the winter hemisphere where it changes sign with height several times, varying from +1 to $-$4 K d^{-1}. It must be remembered that the energy (and momentum) deposition generated by the breaking gravity waves is dependent upon the somewhat arbitrary settings of the parameterization, including the turbulent Prandtl number. Therefore, the reliability of these quantitative estimates is uncertain.

5.2. Momentum Budget

[57] The zonal-mean zonal wind tendencies arising from the parameterized physical processes, as well as from the resolved waves diagnosed using the EPFD, are shown in Figure 10. The vertical diffusion tendency (Figure 10a) includes the effect of both eddy and molecular diffusion. Since vertical diffusion is strongest in regions of strongest wind curvature in the vertical, it will smooth the wind profile. Molecular diffusion acts in the upper part of the model domain together with ion drag (Figure 10b) to reduce model variability by efficiently damping disturbances propagating upward from below. Deceleration of the zonal wind due to molecular diffusion reaches 80 m s^{-1} d^{-1} near 200 km. This is consistent with a viscously dominated thermally direct circulation. The effect of eddy diffusion is seen between 75 and 100 km in the summer hemisphere in the region of the strong reversal of the zonal wind. In this region, it acts against the wind reversal, with a deceleration reaching 20 m s^{-1} d^{-1}.

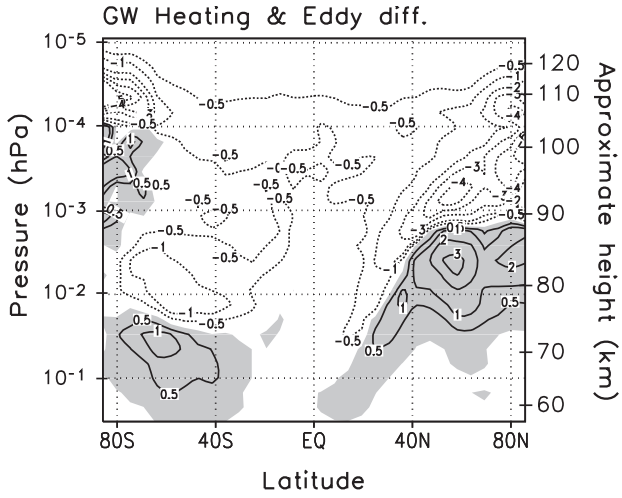

Figure 9. Net thermal effect of gravity-wave breaking in the MLT region for June, combining the effects of gravity-wave heating (Figure 8a) and eddy vertical diffusion (Figure 8b). Positive regions are shaded.

[58] Ion drag (Figure 10b) only acts above 120 km where it grows with altitude, reaching a maximum of up to 250 m s^{-1} d^{-1} near the top of the model in both hemispheres. The effect of ion drag depends solely on wind speed and therefore results in direct deceleration of the zonal flow.

[59] The effect of both the parameterized nonorographic and orographic gravity waves is seen in Figure 10c. The nonorographic gravity-wave drag acts to reverse the mesospheric zonal flow from a westward to an eastward direction in the summer hemisphere and from an eastward to a westward direction in the winter hemisphere. This represents the classical summer-to-winter pole thermally indirect circulation in the MLT region. The net effect of the gravity-wave drag reaches maximum values of +130 m s^{-1} d^{-1} at $\sim$90 km and $-$100 m s^{-1} d^{-1} at $\sim$75 km in the summer and winter hemispheres, respectively. These accelerations are provided mainly by the nonorographic gravity waves. The (stationary) orographic waves cannot penetrate through the critical level in the lower summer stratosphere where westerlies change to easterlies. Therefore orographic gravity-wave drag is important in the middle atmosphere only in wintertime, where it contributes up to $-$20 m s^{-1} d^{-1} near 60–65 km, similar to the values shown by *Beagley et al.* [1997] and *McLandress* [1998].

[60] The CMAM generates a spectrum of waves internally as a result of forcing mechanisms such as large-scale topography, solar and latent heating, jet instabilities, and land/sea temperature contrasts. An analysis of solar tides and planetary waves including the quasi-2-day wave from the extended CMAM has already been done [*McLandress*, 2002]. Detailed analysis of other parts of the wave spectrum will be presented in future publications.

[61] The EPFD diagnostic presented in Figure 10d illustrates the net impact of all resolved waves on the zonal-mean zonal wind and is shown here for comparison with the parameterized momentum tendencies. Above $\sim$120 km, the EPFD is mostly negative in both hemispheres, with maximum values of 80–100 m s^{-1} d^{-1}. In the winter hemisphere (where the zonal wind shown in Figure 4a is eastward), the resolved waves act together with the molecular diffusion and ion drag to decelerate the zonal flow. In the summer hemisphere (where the winds are westward) they act to accelerate the flow, but this effect is largely cancelled by the effects of molecular diffusion and ion drag. In the mesopause region, where the EPFD is positive, the resolved waves enhance the zonal wind reversal produced by the nonorographic gravity waves in summer, but weaken it in winter. This results in a much stronger zonal-wind

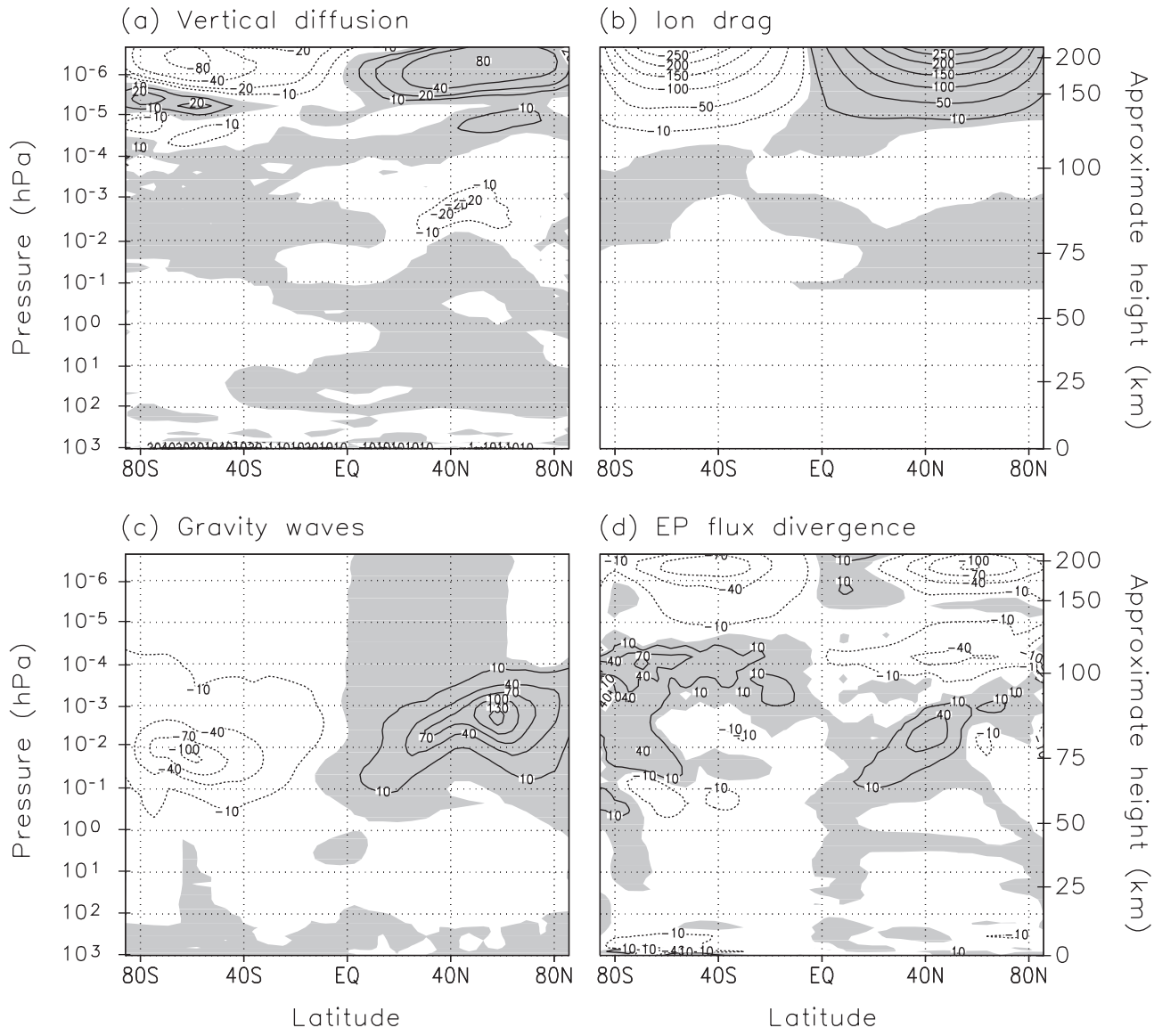

Figure 10. Zonal wind tendency (m s^{-1} d^{-1}) produced by the model in June due to: (a) molecular and eddy vertical diffusion, (b) ion drag, (c) orographic and nonorographic gravity-wave drag, and (c) resolved waves as represented by the Eliassen-Palm flux divergence. Regions of eastward (positive) zonal wind tendency are shaded.

reversal in the upper mesosphere in summer than in winter, as seen in Figure 4a.

6. Summary

[62] This paper has presented a detailed description of the extended version of the Canadian Middle Atmosphere Model (CMAM). The model has been developed by raising the upper boundary of the existing CMAM [*Beagley et al.*, 1997] from ~95 to ~210 km and incorporating new physical processes in the lower thermosphere, with the goal of improving the simulation of the mesosphere/lower thermosphere (MLT) region. The extended CMAM is an atmospheric general circulation model which includes realistic parameterizations of the major physical processes from the ground up to the lower thermosphere, thus providing a very important tool for investigating the coupling between the troposphere and the MLT region. The next step in the model development is to incorporate the interactive neutral chemistry which is currently being used in the standard CMAM [*de Grandpré et al.*, 2000].

[63] As discussed in this paper, the model is capable of producing a reasonable simulation of the zonal-wind distributions as observed by the Upper Atmosphere Research Satellite [*McLandress et al.*, 1996] and temperature as represented in the MSIS-90 temperature model [*Hedin*, 1991]. In particular, the model exhibits a realistic zonal-mean zonal jet reversal in the mesosphere and a reasonable corresponding temperature field. In addition to serving to document the extended version of the CMAM, the paper has also provided a careful examination of the relative importance of the various terms in the energy and momentum budgets, which has never before been done in the MLT region.

[64] The new parameterizations which make it possible to extend the model up to thermospheric heights include solar heating due to absorption by O_3 and O_2 at wavelengths shorter than 0.25 μm and by O_2, N_2, and O in the extreme ultraviolet (EUV) region, a modified parameterization for the 15-μm CO_2 band cooling accounting for the breakdown of local thermodynamic equilibrium conditions, chemical heating due to the atomic oxygen recombination reaction, molecular diffusion and viscosity, ion drag, and the effects of momentum and energy deposition by unresolved non-

orographic gravity waves together with the inclusion of eddy diffusion generated by gravity-wave breaking. The model uses a decoupled infrared cooling scheme that allows the calculation of infrared cooling in the middle and upper atmosphere to be performed every time step, while using a less frequent calculation (every 6 hours) of the computationally intensive tropospheric infrared cooling. This approach considerably improves the numerical stability of the model without any noticeable increase in computational time. Its necessity reflects the very short radiative damping timescales in the upper atmosphere. To avoid using an excessively short time step (which would make long simulations impractical), a height-dependent time filter and enhanced horizontal diffusion in the thermosphere were implemented. These terms do not have a significant direct effect on the budgets shown here.

[65] Analysis of the energy budget reveals two height regions where the pattern of the global and monthly mean energy balance is relatively simple. These are the layer between the tropopause and ~70 km, where radiative equilibrium prevails, and the thermosphere above ~130 km, where the strong EUV solar heating is balanced by molecular diffusion. The pattern is more complicated in the MLT region between 70 and 120 km. In this region, substantial contributions to the energy budget are provided by both chemical heating and dynamical processes. Dynamical processes play a critical role in polar regions, especially during the polar night in the absence of solar heating. The net thermal effect of the parameterized nonorographic gravity waves includes both heating due to direct energy deposition and cooling due to generated thermal eddy diffusion. This effect maximizes in the MLT region near both poles and changes sign with height, being positive below ~70 km and being mostly negative above this level. Although the contribution from nonorographic gravity-wave breaking is important to the energy budget of the polar mesosphere, the main effect produced by the parameterized gravity waves in this region occurs through momentum deposition which results in the well-known zonal wind reversal in the summer mesosphere. Molecular diffusion and ion drag restrain model variability in the upper part of the domain.

Appendix A

[66] This appendix discusses the modifications to the horizontal diffusion and time filter parameters to enhance model stability in the lower thermosphere. The formulation of the horizontal diffusion by subgrid scales that is used in the standard CMAM is described by *Boer et al.* [1984]. This term has been modified to include a height dependence to the parameters. The time tendency is treated in spectral space and is given by

$$\frac{\partial X}{\partial t} = -f(n, z^*)X, \tag{A1}$$

where X is the spectral quantity being diffused (such as vorticity), n is the total horizontal wave number, $z^* \equiv -7\ln(p/1000)$ in kilometers, and p is pressure in mbar. The dissipation function f is given by

$$f = \begin{cases} K[(n - n_{min})/n_{max}]^2, & n > n_{min} \\ 0, & n \le n_{min} \end{cases} \tag{A2}$$

where n_{max} is the truncation wave number (= 32). In the standard CMAM, $K = K_o \equiv 1.2 \times 10^{-4}$ s^{-1} and $n_{min} = n_o \equiv 18$.

[67] This formulation is based on the theory of two-dimensional turbulence [*Leith*, 1971], which is a reasonable supposition for the balanced, vortical, layerwise two-dimensional flow in the troposphere and lower stratosphere. However, *Koshyk et al.* [1999] have shown that middle atmosphere GCMs generically develop a shallow kinetic-energy spectrum at higher altitudes which is associated with the emergence of large-amplitude unbalanced motion. This feature is not too surprising, being simply the resolved part of the gravity-wave spectrum, but it does call for a reconsideration of the horizontal diffusion in order to prevent numerical instability. In the absence of a good understanding of how to represent interactions with subgrid-scale processes for this resolved gravity-wave spectrum, we choose simply to enhance the damping to reflect the much shorter time scale associated with unbalanced motion. Specifically, the damping coefficient K was increased above z_o^* ~113 km (geopotential height $z \sim 103$ km), amplifying the value to a maximum of 50 times its constant value below z_o^* according to

$$K(z^*) = K_o\left[1 + \left(\sqrt{50} - 1\right) * (1 - \exp((z_o^* - z^*)/7))\right]^2 \tag{A3}$$

[$K(z^*) = K_o$, if $z^* \le z_o^*$]. This equation amplifies K rapidly, by an order of magnitude, immediately above z_o^*. (A smoother vertical profile for K has been tested for several months of integration and produces very similar results.) In addition, n_{min} in equation (A1) was also reduced from the value of 18 to 10 above z_o^* according to the equation

$$n_{min}(z^*) = \begin{cases} max\left[n_o exp((z_o^* - z^*)/7, \quad 10\right], & z^* > z_o^* \\ n_o, & z^* \le z_o^* \end{cases} \tag{A4}$$

The above modifications produce damping timescales in the thermosphere of ~2 days, 30 min, and 6 min for wave numbers 11, 20, and 32, respectively.

[68] In the standard version of the CMAM the *Asselin* [1972] time filter is used to suppress computational instabilities that arise from the use of the centered time-differencing scheme. In the extended version it is modified to help suppress high-frequency gravity-wave-like oscillations in the upper mesosphere and thermosphere (which ordinarily require a very short time step in order to not violate the CFL stability criterion). This is done by increasing the filter coefficient μ from its standard value of 0.05 in the lower atmosphere to 0.1 in the thermosphere according to

$$\mu(z^*) = 0.05 + 0.025[1 + \tanh[(z^* - 120)/15]]. \tag{A5}$$

[69] **Acknowledgments.** The authors would like to thank R. G. Roble and R. A. Akmaev for their helpful comments and communications, which are highly appreciated. This work has been supported through the Canadian Middle Atmosphere Modelling project, through grants from the Natural Sciences and Engineering Research Council and the Meteorological Service of Canada.

References

Akmaev, R. A., Simulation of large-scale dynamics in the mesosphere and lower thermosphere with the Doppler-spread parameterization of gravity waves, 1, Implementation and zonal mean climatologies, *J. Geophys. Res.*, *106*, 1193–1204, 2001.

Akmaev, R. A., and V. I. Fomichev, Cooling of the mesosphere and lower thermosphere due to doubling of CO_2, *Ann. Geophys.*, *16*, 1501–1512, 1998.

Akmaev, R. A., V. I. Fomichev, N. M. Gavrilov, and G. M. Shved, Simulation of the zonal mean climatology of the middle atmosphere with a three-dimensional spectral model for solstice and equinox conditions, *J. Atmos. Terr. Phys.*, *54*, 119–128, 1992.

Asselin, R., Frequency filter for time integration, *Mon. Weather Rev.*, *100*, 487–490, 1972.

Banks, P. M., and G. Kockarts, *Aeronomy Part B*, 355 pp., Academic, San Diego, Calif., 1973.

Beagley, S. R., J. de Grandpré, J. N. Koshyk, N. A. McFarlane, and T. G. Shepherd, Radiative-dynamical climatology of the first-generation Canadian middle atmosphere model, *Atmosphere Ocean*, *35*, 293–331, 1997.

Beagley, S. R., C. McLandress, V. I. Fomichev, and W. E. Ward, The extended Canadian middle atmosphere model, *Geophys. Res. Lett.*, *27*, 2529–2532, 2000.

Berger, U., and M. Dameris, Cooling of the upper atmosphere due to CO_2 increases: A model study, *Ann. Geophys.*, *11*, 809–819, 1993.

Boer, G. J., N. A. McFarlane, R. Laprise, J. D. Henderson, and J.-P. Blanchet, The Canadian Climate Centre spectral atmospheric general circulation model, *Atmosphere Ocean*, *22*, 397–429, 1984.

Bougher, S. W., D. M. Hunten, and R. G. Roble, CO_2 cooling in terrestrial planet thermospheres, *J. Geophys. Res.*, *99*, 14,609–14,622, 1994.

Chan, K. L., H. G. Mayr, J. G. Mengel, and I. Harris, A spectral approach for studying middle and upper atmospheric phenomena, *J. Atmos. Terr. Phys.*, *56*, 1399–1419, 1994.

de Grandpré, J., S. R. Beagley, V. I. Fomichev, E. Griffioen, J. C. McConnell, A. S. Medvedev, and T. G. Shepherd, Ozone climatology using interactive chemistry: Results from the Canadian middle atmosphere model, *J. Geophys. Res.*, *105*, 26,475– 26,491, 2000.

Dickinson, R. E., E. C. Ridley, and R. G. Roble, Thermospheric general circulation with coupled dynamics and composition, *J. Atmos. Sci.*, *41*, 205–219, 1984.

Fomichev, V. I., and J.-P. Blanchet, Development of the new CCC/GCM radiation model for extension into the middle atmosphere, *Atmosphere Ocean*, *33*, 513–529, 1995.

Fomichev, V. I., and G. M. Shved, Net radiative heating in the middle atmosphere, *J. Atmos. Terr. Phys.*, *50*, 671–688, 1988.

Fomichev, V. I., and G. M. Shved, On the closeness of the middle atmosphere to the state of radiative equilibrium: An estimation of net dynamical heating, *J. Atmos. Terr. Phys.*, *56*, 479–485, 1994.

Fomichev, V. I., J.-P. Blanchet, and D. S. Turner, Matrix parameterization of the 15 μm CO_2 band cooling in the middle and upper atmosphere for variable CO_2 concentration, *J. Geophys. Res.*, *103*, 11,505–11,528, 1998.

Forbes, J. M., and H. B. Garrett, Solar diurnal tide in the thermosphere, *J. Atmos. Sci.*, *33*, 2226–2241, 1976.

Fouquart, Y., and B. Bonnel, Computation of solar heating of the Earth's atmosphere: A new parameterization, *Beitr. Phys.*, *53*, 35–62, 1980.

Fuller-Rowell, T. G., and D. Rees, A three-dimensional time-dependent global model of the thermosphere, *J. Atmos. Sci.*, *37*, 2545–2567, 1980.

Hays, P. B., V. J. Abreu, M. E. Dobbs, D. A. Gell, H. J. Grassl, and W. R. Skinner, The high-resolution Doppler imager on the Upper Atmosphere Research Satellite, *J. Geophys. Res.*, *98*, 10,713–10,723, 1993.

Hedin, A. E., Extension of the MSIS thermospheric model into the middle and lower atmosphere, *J. Geophys. Res.*, *96*, 1159–1172, 1991.

Hines, C. O., Doppler-spread parameterization of gravity-wave momentum deposition in the middle atmosphere, Part 1, Basic formulation, *J. Atmos. Sol.-Terr. Phys.*, *59*, 371–386, 1997a.

Hines, C. O., Doppler-spread parameterization of gravity-wave momentum deposition in the middle atmosphere. Part 2: Broad and quasi-monochromatic spectra, and implementation, *J. Atmos. Sol. Terr. Phys.*, *59*, 387–400, 1997b.

Hines, C. O., Correction to "Doppler-spread parameterization of gravity-wave momentum deposition in the middle atmosphere, Part 1, Basic formulation," *J. Atmos. Sol. Terr. Phys.*, *61*, 941, 1999.

Hong, S.-S., and R. S. Lindzen, Solar semidiurnal tide in the thermosphere, *J. Atmos. Sci.*, *33*, 135–153, 1976.

Kockarts, G., Nitric oxide cooling in the terrestrial thermosphere, *Geophys. Res. Lett.*, *7*, 137–140, 1980.

Koshyk, J. N., B. A. Boville, K. Hamilton, E. Manzini, and K. Shibata, Kinetic energy spectrum of horizontal motions in middle-atmosphere models, *J. Geophys. Res.*, *104*, 27,177–27,190, 1999.

Leith, C. E., Atmospheric predictability and two-dimensional turbulence, *J. Atmos. Sci.*, *28*, 145–161, 1971.

McFarlane, N. A., The effect of orographically excited gravity wave drag on the general circulation of the lower stratosphere and troposphere, *J. Atmos. Sci.*, *44*, 1775–1800, 1987.

McFarlane, N. A., G. J. Boer, J.-P. Blanchet, and M. Lazare, The Canadian Climate Center second-generation general circulation model and its equilibrium climate, *J. Clim.*, *5*, 1013–1044, 1992.

McIntyre, M. E., On dynamics and transport near the polar mesopause in summer, *J. Geophys. Res.*, *94*, 14,617–14,628, 1989.

McLandress, C., Seasonal variability of the diurnal tide: Results from the Canadian middle atmosphere general circulation model, *J. Geophys. Res.*, *102*, 29,747–29,764, 1997.

McLandress, C., On the importance of gravity waves in the middle atmosphere and their parameterization in general circulation models, *J. Atmos. Sol.-Terr. Phys.*, *60*, 1357–1383, 1998.

McLandress, C., The seasonal variation of the propagating diurnal tide in the mesosphere and lower thermosphere, Part I, The role of gravity waves and planetary waves, *J. Atmos. Sci.*, *59*, 893–906, 2002.

McLandress, C., G. G. Shepherd, B. H. Solheim, M .D. Burrage, P. B. Hays, and W. R. Skinner, Combined mesosphere/thermosphere winds using WINDII and HRDI data from the Upper Atmosphere Research Satellite, *J. Geophys. Res.*, *101*, 10,441–10,453, 1996.

Miyahara, S., and Y. Miyoshi, Migrating and non-migrating atmospheric tides simulated by a middle atmosphere general circulation model, *Adv. Space Res.*, *20*, 1201–1207, 1997.

Miyahara, S., Y. Yoshida, and Y. Miyoshi, Dynamic coupling between the lower and upper atmosphere by tides and gravity waves, *J. Atmos. Terr. Phys.*, *55*, 1039–1053, 1993.

Mlynczak, M. G., and S. Solomon, A detailed evaluation of the heating efficiency in the middle atmosphere, *J. Geophys. Res.*, *98*, 10,517–10,541, 1993.

Morcrette, J.-J., Radiation and cloud radiative properties in the ECMWF operational weather forecast model, *J. Geophys. Res.*, *96*, 9121–9132, 1991.

Norton, W. A., and J. Thuburn, The mesosphere in the extended UGAMP GCM, in *Gravity Wave Processes and Their Parameterization in Global Climate Models*, NATO ASI vol. 50, edited by K. Hamilton, pp. 383–401, Springer-Verlag, New York, 1997.

Norton, W. A., and J. Thuburn, Sensitivity of mesospheric mean flow, planetary waves, and tides to strength of gravity wave drag, *J. Geophys. Res.*, *104*, 30,897–30,911, 1999.

Ogibalov, V. P., V. I. Fomichev, and A. A. Kutepov, Radiative heating effected by infrared CO_2 bands in the middle and upper atmosphere, *Atmos. Oceanic Phys.*, *36*, 454–464, 2000.

Pawson, S., et al., The GCM-reality Intercomparison project for SPARC: Scientific issues and initial results, *Bull. Amer. Meteorol. Soc.*, *81*, 781–796, 2000.

Richards, P. G., J. A. Fennelly, and D. G. Torr, EUVAC: A solar EUV flux model for aeronomic calculations, *J. Geophys. Res.*, *99*, 8981–8992, 1994. (Correction, *J. Geophys. Res., 99,* 13,283, 1994.)

Richmond, A. D., The neutral upper atmosphere, in *Geomagnetism*, edited by J. A. Jacobs, vol. 4, pp. 403–479, Academic, San Diego, Calif., 1991.

Riese, M., R. Spang, P. Preusse, M. Ern, M. Jarisch, D. Offermann, and K. U. Grossmann, Cryogenic Infrared Spectrometers and Telescopes for the Atmosphere (CRISTA) limb scan measurements, data processing, and atmospheric temperature and trace gas retrieval, *J. Geophys. Res.*, *104*, 16,349–16,367, 1999.

Roble, R. G., Energetics of the Mesosphere and Thermosphere, in *The Upper Mesosphere and Lower Thermosphere: A Review of Experiment and Theory*, *Geophys. Monogr. Ser.*, vol. 87, edited by R. M. Johnson and T. L. Killeen, pp. 1– 21, AGU, Washington, D. C., 1995.

Roble, R. G., and E. C. Ridley, A thermosphere-ionosphere-mesosphere electrodynamics general circulation model (TIME-GCM): Equinox solar cycle minimum simulations (30–500 km), *Geophys. Res. Lett.*, *21*, 417–420, 1994.

Roble, R. G., E. C. Ridley, and R. E. Dickinson, On the global mean structure of the thermosphere, *J. Geophys. Res.*, *92*, 8745–8758, 1987.

Shepherd, G. G., et al., WINDII, the Wind Imaging Interferometer on the Upper Atmosphere Research Satellite, *J. Geophys. Res.*, *98*, 10,725–10,750, 1993.

Shepherd, T. G., K. Semeniuk, and J. N. Koshyk, Sponge-layer feedbacks in middle atmosphere models, *J. Geophys. Res.*, *101*, 23,447–23,464, 1996.

Strobel, D. F., Parameterization of the atmospheric heating rate from 15 to 120 km due to O_2 and O_3 absorption of solar radiation, *J. Geophys. Res.*, *83*, 6225–6230, 1978.

Wilcox, R. W., and A.D. Belmont, Ozone concentration by latitude, altitude and month near 80W, *Rep. FAA-AEQ-77-13*, U.S. Dep. of Transport., FAA Off. of Environ. Qual., High Altitude Pollut. Program, Washington, D. C., 1977.

S. R. Beagley, V. I. Fomichev, and J. C. McConnell, Department of Earth and Atmospheric Science, York University, 4700 Keele Street, Toronto, Ontario, Canada M3J 1P3. (victor@nimbus.yorku.ca; beagley@nimbus.yorku.ca; jack@nimbus.yorku.ca)

N. A. McFarlane, University of Victoria, P.O. Box 1700, Victoria, BC, Canada V8W 2Y2. (Norm.McFarlane@ec.gc.ca)

C. McLandress and T. G. Shepherd, Department of Physics, University of Toronto, Toronto, Ontario, Canada M5S 1A7. (charles@mam.physics.utoronto.ca; tgs@atmosp.physics.utoronto.ca)

W. E. Ward, Department of Physics, University of New Brunswick, P.O. Box 4400, Fredericton, N.B., Canada E3B 5A3. (wward@unb.ca)